RSC Advances

PAPER

Cite this: *RSC Adv.*, 2017, 7, 29481

Synthesis and electrochemical performance of NaV_6O_{15} microflowers for lithium and sodium ion batteries†

Fang Hu,[a] Wei Jiang,[a] Yidi Dong,[a] Xiaoyong Lai,[b] Li Xiao[a] and Xiang Wu*[a]

Hierarchical NaV_6O_{15} flower-like structures were successfully synthesized *via* a facile hydrothermal reaction combined with subsequent thermal transformation. The as-prepared NaV_6O_{15} microflowers are composed of many nanoneedles with a width of about 200 nm and a length of several micrometers. The electrochemical performance of NaV_6O_{15} microflowers as cathodes for both lithium and sodium ion batteries are investigated. High first discharge capacities of 255 mA h g^{-1} (*vs.* Li^+/Li) and 130 mA h g^{-1} (*vs.* Na^+/Na) are observed and the capacity retention reaches 105% and 64% after 50 cycles under 4–1.5 V at a current density of 100 mA g^{-1} and 50 mA g^{-1}, respectively. High lithium/sodium ion diffusion coefficients play an important role in improving the electrochemical performance of NaV_6O_{15} microflowers.

Received 19th April 2017
Accepted 31st May 2017

DOI: 10.1039/c7ra04388k

rsc.li/rsc-advances

1. Introduction

Recently, there has been increasing interest in rechargeable lithium-ion batteries (LIBs) and sodium-ion batteries (NIBs) because of their inherent advantages such as high specific energy density, long cycle life as well as environmental benignity.[1–8] Especially, due to abundant sodium resources and potential low cost, NIBs have attracted much interest as an alternative to LIBs in large scale energy storage systems[9,10] However, Na^+ has a larger size (1.06 Å) than that of Li^+ (0.76 Å), which makes it difficult for sodium ions to quickly insert/extract from the host materials.[11] As a result, most common electrode materials for LIBs are unsuitable to accommodate sodium ions.[12–15] Therefore, it is of great importance to develop new electrode materials for both LIBs and SIBs.

Vanadium oxide possesses good reactive activity because of its variable oxidation states from +5 in V_2O_5 to +2 in VO. Especially, V_2O_5 could present various phase transformations during Li^+/Na^+ intercalation/deintercalation process. For different intercalated amounts of Li^+/Na^+, the theoretical capacities is up to 442 mA h g^{-1} and 236 mA h g^{-1} for $Li_3V_2O_5$ and $Na_2V_2O_5$, respectively. However, $Li_xV_2O_5$ or $Na_xV_2O_5$ with an intercalated amount $x > 1$ suffers a significant capacity loss during Li^+/Na^+ intercalation/deintercalation process, leading to a poor cycling performance.[16,17] A possible strategy is to introduce second metal cations, such as Na^+ and $NH_4{}^+$, into V_2O_5 interlayer, which could support V_2O_5 layers as "pillars" and generate a fast Li^+/Na^+ diffusion path.[18–20] At present, many types of synthesis methods for NaV_6O_{15} (β-$Na_{0.33}V_2O_5$), such as solid–state reaction,[21] sol–gel method[22] and hydrothermal method,[23,24] have been attempted to improve its electrochemical performances. Among various morphologies of NaV_6O_{15} structures, nanosheets,[25] microspheres[26] and nanoflakes,[27] can improve electrochemical performance of the batteries further. For example, Lu *et al.* reported hydrothermal synthesis of β-$Na_{0.33}V_2O_5$ nanosheets, which exhibited a discharge capacity of 258 mA h g^{-1} at the current density of 150 mA g^{-1} and the capacity retention of 70.2% after 50 cycles.[25] Wang and his coworkers prepared β-$Na_{0.33}V_2O_5$ nanorods, which delivered desirable discharge capacity of 223.9 mA h g^{-1} at 60 mA g^{-1} with high capacity retention of 81.3% after 50 cycles.[28] Jiang's group obtained NaV_6O_{15} nanoplates with a discharge capacity of 116 mA h g^{-1} (*vs.* Na^+/Na) and a cycle retention of 55% after 30 cycles at the current density of 50 mA g^{-1}.[29]

Herein, we report novel hierarchical NaV_6O_{15} microflowers synthesized by a facile hydrothermal reaction combined with subsequent thermal transformation. Electrochemical properties of NaV_6O_{15} microflowers as cathodes for both lithium and sodium ion batteries are investigated. High first discharge capacity of 255 mA h g^{-1} (*vs.* Li^+/Li) and 130 mA h g^{-1} (*vs.* Na^+/Na) are observed and capacity retentions reach 105% and 64% after 50 cycles under 4–1.5 V at the current density of 100 mA g^{-1} and 50 mA g^{-1}, respectively. More importantly, Li/Na ion diffusion coefficients of NaV_6O_{15} cathode material is proposed and verified.

2. Experimental

All the reagents were of analytical grade and used without further purification. In a typical procedure, 0.24 g NaOH,

---

[a] *School of Materials Science and Engineering, Shenyang University of Technology, Shenyang 110870, P. R. China. E-mail: wuxiang05@163.com; wuxiang05@sut.edu.cn*

[b] *State Key Laboratory of High-efficiency Utilization of Coal and Green Chemical Engineering, College of Chemistry and Chemical Engineering, Ningxia University, Yinchuan 750021, P. R. China*

† Electronic supplementary information (ESI) available. See DOI: 10.1039/c7ra04388k

0.234 g NH_4VO_3 and 0.053 g Na_2CO_3 were added together to a beaker with 50 mL of distilled water and the solution was stirred at 90 °C for 20 min. Then, put the beaker into cool water. 1 mL 3% H_2O_2 was dissolved in the solution and stirred about 2 min. The solution was adjusted to pH ≈ 2 by the titration of 2 mol L^{-1} HCl and kept for stirring about 30 min. Finally, the orange solution was thrown into a 50 mL autoclave and subjected to hydrothermal treatment at 200 °C for 24 h. And then, the autoclave was naturally cooled down and yellow precipitates were collected, followed with wash with distilled water and alcohol for several times, and finally dried at 110 °C. The resultant product was heated in air atmosphere at 400 °C for 4 h with an increasing rate of 3 °C min^{-1}.

The powder X-ray diffraction (XRD) patterns were obtained by an XRD-7000 diffractometer attached with Cu Kα radiation. The scan step was 6° min^{-1} and the tube current and voltage were 30 mA and 40 kV, respectively. Scanning electron microscope (SEM) images were recorded by a JSM-6700F, operated at 5.0 kV. Transmission electron microscope (TEM) images were obtained by an FEI Tecnai G2. The nitrogen adsorption–desorption isotherms at the temperature of liquid nitrogen (77 K) were measured on VSorb 4800P Surface Area and Pore Porosimetry Analyzer (Gold Spectrum Technology Co., Ltd., China) with prior degassing under vacuum for 4 h at 200 °C. Total pore volumes were determined using the adsorbed volume at a relative pressure of 0.99. The multi-point Brunauer–Emmett–Teller (BET) surface area was estimated from the relative pressure range from 0.05 to 0.2. The pore size distribution of all the materials was analyzed from the desorption isotherm using the Barrett–Joyner–Halenda (BJH) method.

Electrochemical tests were performed by using a coin battery cell, where a metallic lithium foil was used as the anode electrode. NaV_6O_{15} active material (80%, mass fraction) were blended with acetylene black (10%, mass fraction) and polyvinylidenefluoride (PVDF, 10%, mass fraction). The resultant slurry was pasted on an Al foil as cathode electrode and then dried in a vacuum oven. Each electrode (8 × 8 mm^2) contain 2 mg of active material. 1 mol L^{-1} lithium hexafluorophosphate ($LiPF_6$) dissolved in ethylene carbonate (EC), dimethyl carbonate (DMC) and ethyl methyl carbonate (EMC) (EC : DMC : EMC = 1 : 1 : 8, by v/v ratio) was used as electrolyte. For Na coin cells, the electrolyte was 1 mol L^{-1} $NaClO_4$ dissolved in a solvent mixture of ethylene carbonate (EC) and propylene carbonate (PC) (1 : 1 v/v) and 5% FEC. Galvanostatic charge–discharge cycling was carried out with an automatic battery tester (Land-2100, China) in the voltage window of 1.5–4.0 V. Cyclic voltammetry was performed with a VSP multichannel potentiostatic–galvanostatic system (Bio-Logic) at a scanning rate of 0.05, 0.1, 0.15, 0.2, 0.25 and 0.3 mV s^{-1}, respectively.

3. Results and discussion

XRD patterns of the as-synthesized precursor and resultant NaV_6O_{15} product are showed in Fig. 1, respectively. The diffraction peaks of the as-synthesized precursor could be well indexed to $HNaV_6O_{16}\cdot4H_2O$ phase (JCPDS no. 49-0996) except for an unknown diffraction peak at about $2\theta = 26.9°$. After heated at 400 °C, all the peaks can be well indexed to monoclinic layered NaV_6O_{15} phase (JCPDS No. 24-1155), and no other impurities are detected.

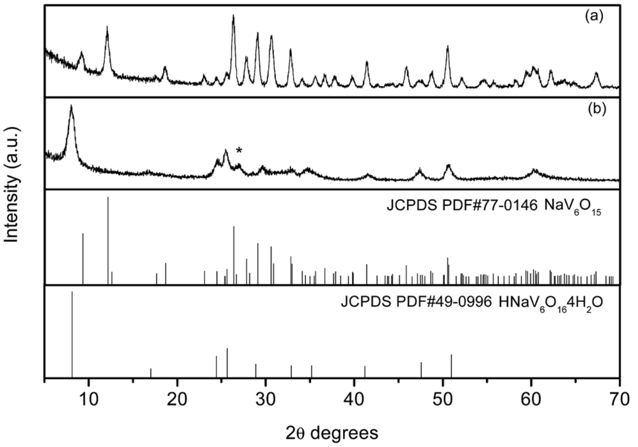

Fig. 1 XRD patterns of the as-synthesized precursor and NaV_6O_{15} products.

General SEM images of $HNaV_6O_{16}\cdot4H_2O$ and NaV_6O_{15} samples are shown in Fig. 2a. $HNaV_6O_{16}\cdot4H_2O$ are mainly some microflowers with a diameter of about 5 μm. High magnification SEM images in Fig. 2b shows the microflowers are composed of some nanobelts with a width of about 100 nm and a length of several micrometers. Fig. 2c and d show SEM images of NaV_6O_{15} sample, which reveal that the nanobelts are melt to nanoneedles-like with a width of about 200 nm. After calcined at 500 °C, NaV_6O_{15} microflowers are melted further to microcrystals with the size of about 1 μm (Fig. S1†). NaV_6O_{15} microflowers are further investigated by TEM as shown in Fig. 3. The distance between the neighboring fringes is about 0.364 nm, which is consistent with that of the (004) plane of monoclinic layered NaV_6O_{15}. The mappings of different elements from NaV_6O_{15} microflowers are shown in Fig. 3c. It shows that Na, V and O elements are all uniformly distributed.

Nitrogen adsorption–desorption isotherms and the corresponding pore size distribution curves of NaV_6O_{15} microflowers is shown in Fig. 4. The isothermal curve is of typical IV type, which indicates the porous characteristic of NaV_6O_{15} microflowers. According to multi-point BET method, a high specific surface area of 54 m^2 g^{-1} is achieved with an average pore size of 6.4 nm and a large pore volume of 0.15 cm^3 g^{-1}. It is well known that nanoscale materials with high surface area can decreases effective diffusion path and increases surface area for insertion and extraction of Li^+/Na^+, all of which are beneficial to the battery performance.[30,31]

Galvanostatic charge–discharge profiles of $HNaV_6O_{16}\cdot4H_2O$ and NaV_6O_{15} microflowers are examined at a current density of 100 mA g^{-1} with Li in the voltage range from 4 V to 1.5 V, as presented in Fig. 5a. It can be observed that $HNaV_6O_{16}\cdot4H_2O$ microflowers electrode presents almost no electrochemical performance. NaV_6O_{15} microflowers give a high discharge capacity of 255 mA h g^{-1}, which is larger than that of NaV_6O_{15} powders calcined at 500 °C (Fig. S2a†). From the cyclic

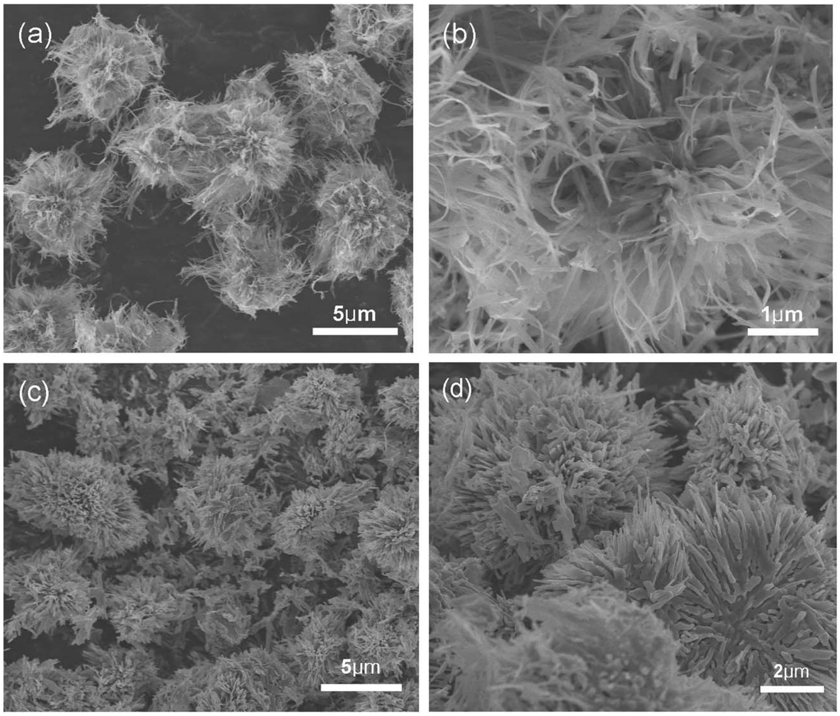

Fig. 2 SEM images of $HNaV_6O_{16}\cdot 4H_2O$ (a and b) and NaV_6O_{15} samples (c and d).

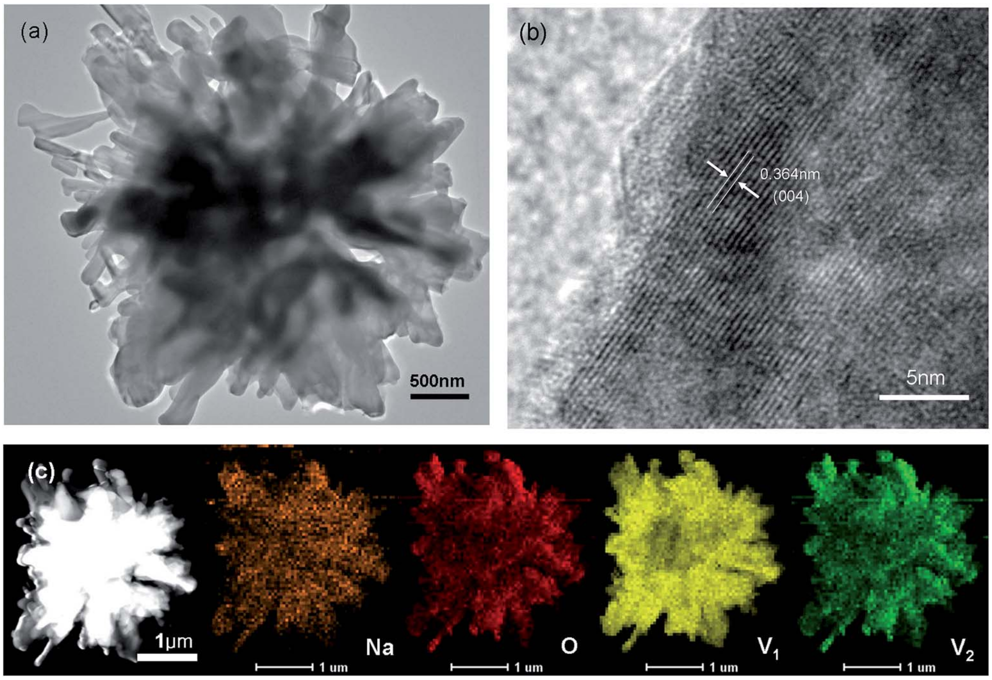

Fig. 3 TEM (a) and HRTEM (b) of NaV_6O_{15} microflowers (c) mapping of NaV_6O_{15} microflowers.

voltammetry curves of NaV_6O_{15} microflowers (inset of Fig. 5a) at a scan rate of 0.05 mV s^{-1} from 1.5 to 4.0 V, there are four plateaus at 3.25 V, 2.88 V, 2.49 V and 1.97 V, indicating multi-step intercalation of Li^+ ions and corresponding to Li contents of $0 < x \leq 0.33$, $0.33 < x \leq 0.66$, $0.66 < x \leq 1.67$ and $1.67 < x \leq 2.0$, respectively.[32] Voltage profiles of first Li^+ ion intercalation plateau are relatively lower than those in subsequent intercalation processes (Fig. 5b). It might be due to successive and reversible phase transformations in the cathode materials during the insertion/extraction and stress/strain, whereas a large volume expansion in the first insertion result in large strain over-potential.[33] The second discharge capacity is about

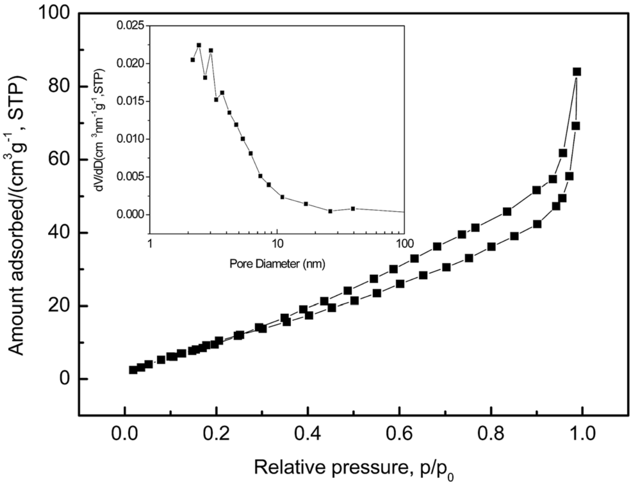

Fig. 4 Nitrogen adsorption–desorption isotherms and pore size distribution curves (in set) of NaV_6O_{15} microflowers.

280 mA h g^{-1}, which is higher than the first, revealing that a part of extra charge capacity is attributed to the extraction of Na^+ ions from the host material, which is similar to that of $Na_5V_{12}O_{32}$.[33] Therefore, more Li^+ can be inserted into the host material in the next curves. All of the charge–discharge profiles in Fig. 5b show similar multistep discharge/charge behaviors, suggesting a highly reversible process of Li^+ ion intercalation and deintercalation in NaV_6O_{15} microflowers. After 50 cycles (Fig. 5c), NaV_6O_{15} microflowers can maintain discharge capacities of 268 mA h g^{-1} at 100 mA g^{-1} with high coulombic efficiency of about 98% and high capacity retention of about 105%. For comparison, electrochemical properties of NaV_6O_{15} microflowers and other work with Li were summarized in Table 1. It can be seen that NaV_6O_{15} micromicroflowers show outstanding electrochemical performance. Fig. 5d shows rate performance of NaV_6O_{15} microflowers at different current densities. At the current densities of 100 mA g^{-1}, 200 mA g^{-1}, 400 mA g^{-1}, 800 mA g^{-1} and 1600 mA g^{-1}, NaV_6O_{15} microflowers exhibit discharge capacities of 250 mA h g^{-1}, 237 mA h g^{-1}, 195 mA h g^{-1}, 142 mA h g^{-1} and 81.2 mA h g^{-1}, respectively. When cycling at 100 mA h g^{-1} again, the discharge capacity remains at 233 mA h g^{-1}, which indicates NaV_6O_{15} microflowers cathode remains stable after high rates.

To further understand the electrochemical kinetics, cyclic voltammetry curves of the electrodes at different voltage scan rates with Li were show in Fig. 6a. The Li^+ diffusion coefficient (D_{Li}) of the material was calculated according to eqn (1).

$$I_p = 2.69 \times 10^5 n^{3/2} AD^{1/2} v^{1/2} C \tag{1}$$

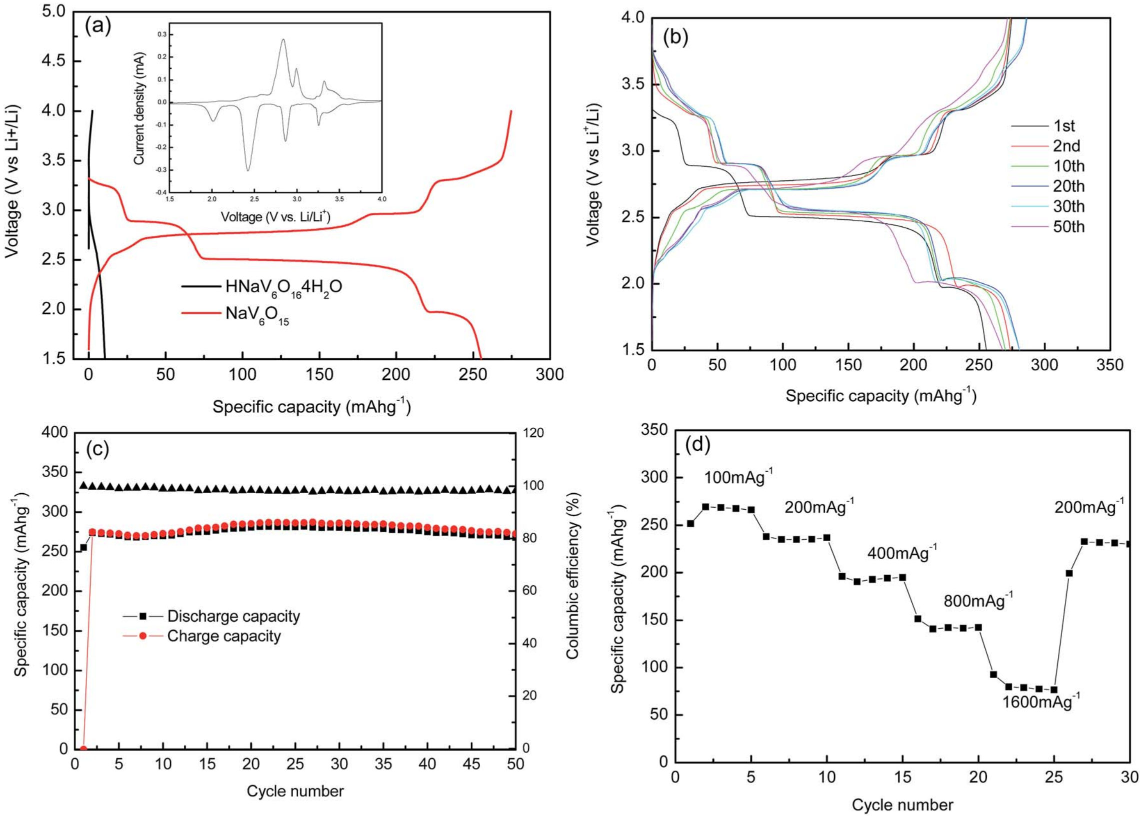

Fig. 5 (a) First charge–discharge profiles of $HNaV_6O_{16}\cdot 4H_2O$ and NaV_6O_{15} microflowers, the inset is CV curves of NaV_6O_{15}/Li (b) discharge/charge profiles of the selected cycles at the current density of 100 mA g^{-1} (c) cycling performance of the electrodes at the current density of 100 mA g^{-1} and the corresponding coulombic efficiency (d) rate performance tested at different current densities.

Table 1 Comparison on electrochemical performance of NaV_6O_{15} microflowers and other sodium vanadates as cathode material for LIBs

Composition	Current density ($mA\ g^{-1}$)	First discharge capacity ($mA\ h\ g^{-1}$)	Cycle numbers	Capacity and retension ($mA\ h\ g^{-1}$)	Li-ion batteries	Ref.
Rod-shaped β-$Na_{0.33}V_2O_5$	3.8	284	70	253 (89%)	Li^+/Li	23
Mesoporous β-$Na_{0.33}V_2O_5$	20	339	50	177 (60.2%)	Li^+/Li	23
$Na_{0.33}V_2O_5$ nanosheets	150	258	50	181 (70.2%)	Li^+/Li	25
β-$Na_{0.33}V_2O_5$ nanorods	60	224	50	182 (81.3%)	Li^+/Li	28
$Na_{0.33}V_2O_5$ micro rod	17	297	50	295 (99%)	Li^+/Li	32
Rice-shaped $Na_{1.08}V_6O_{15}$	30	302	100	205 (68%)	Li^+/Li	34
NaV_6O_{15} nanoflowers	100	255	50	268 (105%)	Li^+/Li	This work

(n, electron number per specific reaction (for Li^+ $n = 1$); A, electrode surface area, about 0.64 cm^2 in this work; C, Li ion concentration in the sample; I_p, current intensity; v, scan rate). I_p varies linearly with $v^{1/2}$ as shown in Fig. 6b and c. The lithium diffusion coefficients could be calculated by using eqn (1) (Fig. 6d). Li ions diffusion coefficient is about 5.6×10^{-11} to 7.3×10^{-13} $cm^2\ s^{-1}$, which is better than that of rod-shaped $Na_{0.33}V_2O_5$.[21] It may be attributed to porous structure of NaV_6O_{15} microflowers, which could shorten the effective diffusion path and increase the window numbers for insertion and extraction of Li^+. In addition, the Li ions diffusion coefficient (D_{Li}) of NaV_6O_{15} microflowers showed a decrease during the discharge process, indicating that the diffusion of Li^+ in the electrode becomes more difficult, possibly resulted from the puckering $[V_6O_{15}]$ layers as well as the corresponding structural transformation.

The electrochemical performance of NaV_6O_{15} microflowers as cathode material for Na-ion batteries was also investigated. Fig. 7a shows charge–discharge profiles of $HNaV_6O_{16}\cdot 4H_2O$ and NaV_6O_{15} microflowers at a current density of 50 mA g^{-1} with Na in the voltage range from 4 V to 1.5 V. It also can be observed that the $HNaV_6O_{16}\cdot 4H_2O$ microflowers electrode presents little electrochemical performance. NaV_6O_{15} microflowers delivers a first discharge capacity of about 130 mA h g^{-1}, which is also higher than that of NaV_6O_{15} powders (Fig. S2b†). The cyclic voltammetry curves of NaV_6O_{15}

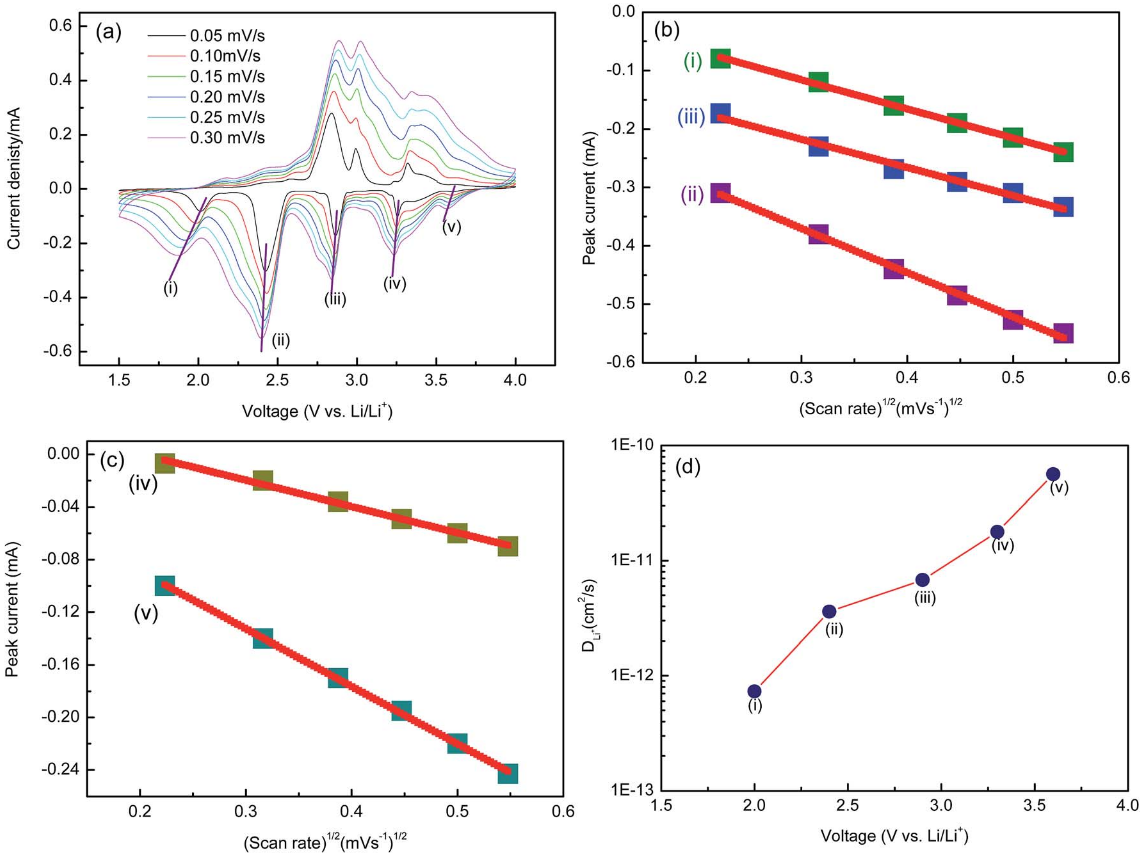

Fig. 6 (a) CV curves of the NaV_6O_{15} microflowers at different voltage scan rates with Li (b) and (c) linear fitting of the I_p *versus* $v^{1/2}$ relationships for LIBs (d) diffusion coefficients of Li^+ in NaV_6O_{15} microflowers at different charge states.

microflowers (in inset of Fig. 7a) at a scan rate of 0.05 mV s^{-1} from 1.5 to 4.0 V shows three obvious anodic peaks at 2.08, 2.49 and 2.95 V and two cathodic peaks at 2.67 and 1.71 V. Interestingly, NaV_6O_{15} product shows different work plateaus between 4.0 and 1.5 V in the LIBs or SIBs, which can be understood by the complex structural transitions upon Li^+/Na^+ insertion with different ionic radius.[34] In the subsequent charge–discharge processes, the discharge plateau at about 2.67 V in the first cycle disappears and the discharge capacity reduces to 115 mA h g^{-1}, which might be related to the structure rearrangement of NaV_6O_{15} in the first Na ion intercalation. In the next few cycles, higher capacity can be attributed to the incomplete electrochemical reaction because of flowerlike morphology and inadequate contact with electrolyte.

After 50 cycles, the discharge capacity of 83 mA h g^{-1} is maintained with the retention of 64% and the coulombic efficiency of 82% (Fig. 7c). Compared to NaV_6O_{15}/Li, good cycle performance of NaV_6O_{15}/Li may be due to that Na ions in NaV_6O_{15} structure are thought to be immobile and to act as a pillar between the $[V_6O_{15}]$ layers, which prevent the structural collapse of NaV_6O_{15} during charge/discharge cycling. In NaV_6O_{15}/Na, Na^+ will not act as the pillar again and the extensive discharge depth to 1.5 V brings about a collapse of the crystallographic structure of the sample.[35] Nevertheless, NaV_6O_{15} microflowers shows good cycle performance when it was used as a cathode material for Na-ion batteries, superior over those reported in early literatures (Table 2).

Short cycling performance of NaV_6O_{15} microflowers at different current rates from 50 to 800 mA g^{-1} is shown in Fig. 7d. The electrode presents good rate capability with high reversible discharge capabilities of 125 mA h g^{-1}, 112 mA h g^{-1}, 90 mA h g^{-1}, 64 mA h g^{-1} and 38 mA h g^{-1} at the current densities of 50 mA g^{-1}, 100 mA g^{-1}, 200 mA g^{-1}, 400 mA g^{-1} and 800 mA g^{-1}, respectively. In Fig. 8a, cyclic voltammetry in different scan rates was also utilized to determine the Na^+ diffusion coefficient (D_{Na}) of the sample, and I_p varies linearly with $v^{1/2}$ is shown in Fig. 8b. On this basis, one can calculate Na ions diffusion coefficients according to eqn (1) is about 1.37×10^{-13} to 4.87×10^{-13} cm^2 s^{-1}, which is close to the results of Electrochemical Impedance Spectroscopy (EIS).[36,37] The result shows that the value of D_{Na} for NaV_6O_{15} sample obtained is higher than that of olivine $NaFePO_4$ (8.7×10^{-17} cm^2 s^{-1}),[38] which shows potential application as a cathode candidate for NIBs with high performance.

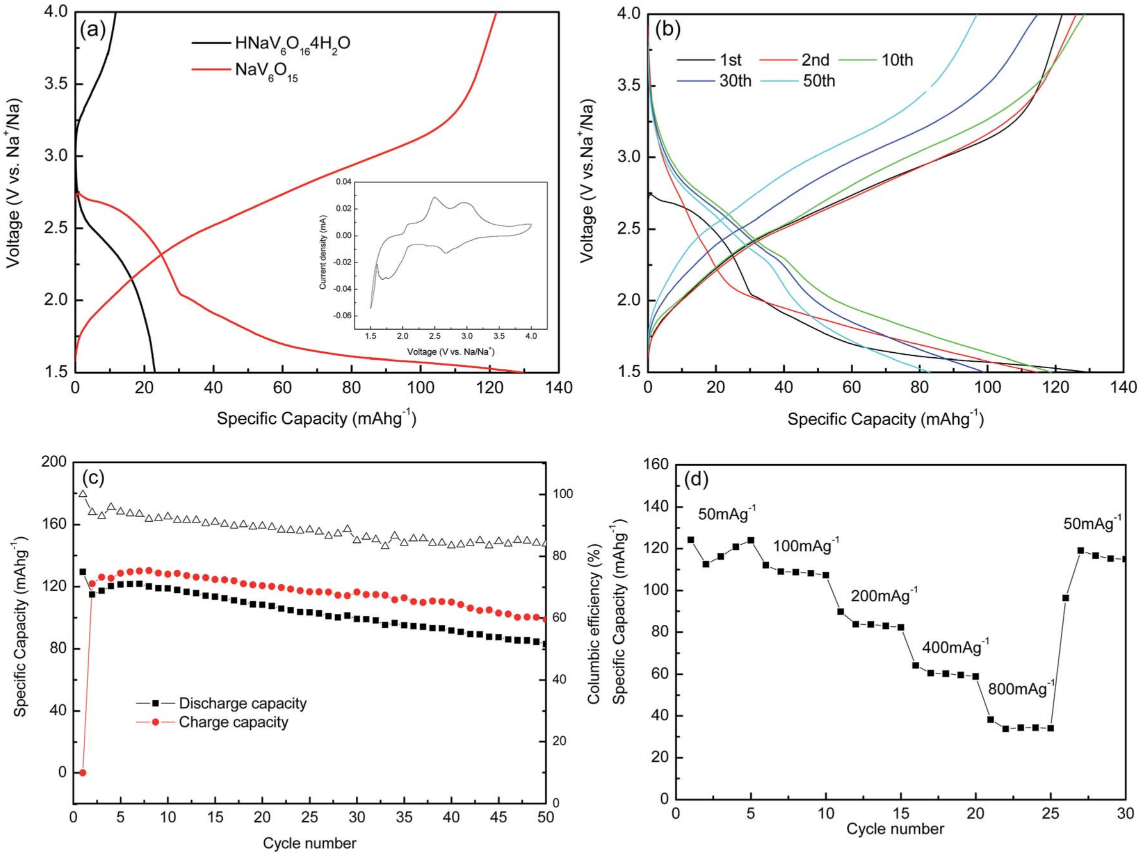

Fig. 7 (a) First charge–discharge profiles of $HNaV_6O_{16}\cdot 4H_2O$ and NaV_6O_{15} microflowers, the inset is CV curves of NaV_6O_{15}/Na (b) discharge/charge profiles of the selected cycles at the current density of 50 mA g^{-1} (c) cycling performance of NaV_6O_{15} microflowers at the current density of 50 mA g^{-1} and the corresponding coulombic efficiency; (d) rate performance tested at different current densities.

Table 2 Comparison on electrochemical performance of NaV_6O_{15} microflowers and other sodium vanadates as cathode material for NIBs

Composition	Current density (mA g^{-1})	First discharge capacity (mA h g^{-1})	Cycle numbers	Capacity and retension (mA h g^{-1})	Na-ion batteries	Ref.
NaV_6O_{15} nanoflakes	15	148	30	136 (92.2%)	Na^{+}/Na	27
NaV_6O_{15} nanoplates	50	116	30	63.8 (55%)	Na^{+}/Na	29
NaV_6O_{15} nanorods	50	106	30	75 (71%)	Na^{+}/Na	35
NaV_6O_{15} nanorods	50	134	20	96.5 (72%)	Na^{+}/Na	36
$Na_{0.33}V_2O_5$ nanosheets	20	188.4	50	97.8 (51.9%)	Na^{+}/Na	37
NaV_6O_{15} nanoflowers	50	130	30	100 (77%)	Na^{+}/Na	This work
			50	83 (64%)		

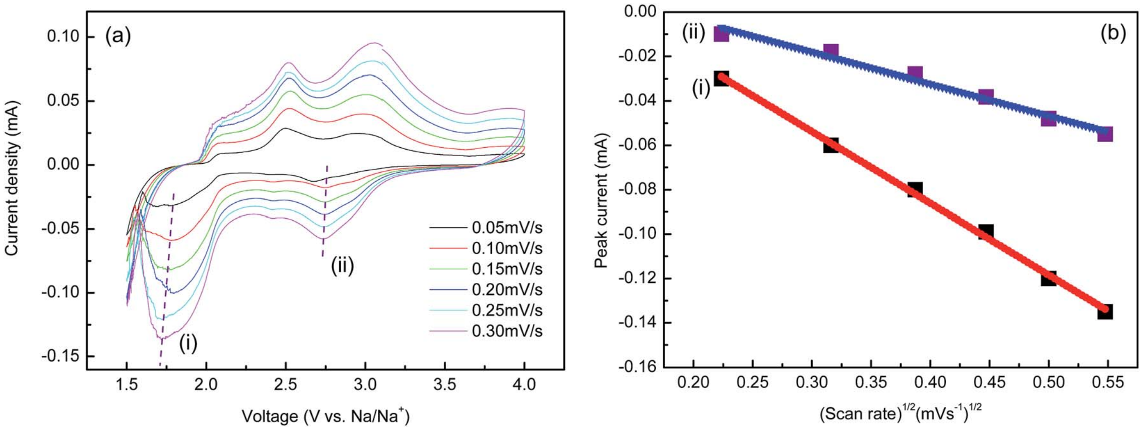

Fig. 8 (a) CV curves of NaV_6O_{15} microflowers at different voltage scan rates with Na (b) linear fitting of the I_p *versus* $\upsilon^{1/2}$ relationships.

4. Conclusions

In summary, NaV_6O_{15} microflowers have been successfully synthesized using a simple hydrothermal method with subsequent annealing treatment. The as-synthesized NaV_6O_{15} microflowers are investigated as cathodes for both LIBs and SIBs, which exhibited good electrochemical storage performance. According to cyclic voltammetry analysis at different voltage scan rates, Li/Na, the Li/Na ions diffusion coefficients is about 10^{-11} and 10^{-13} cm^2 s^{-1}, respectively. High Li/Na ions diffusion coefficients would be responsible for remarkable electrochemical performance of NaV_6O_{15} microflowers.

Acknowledgements

This work was supported Foundation of state Key Laboratory of high effciency Utilization of Coal and Green Chemical Engineering (Grant No. 2016-19), initial funding for top level talents of Shenyang University of Technology and Nature Science Fund of Liaoning province (No. 20170540671).

References

1 D. X. Wang, Q. Liu, C. J. Chen, M. L. Li, X. Meng, X. F. Bei, Y. J. Wei, Y. H. Huang, F. Du and C. Z. Wang, *ACS Appl. Mater. Interfaces*, 2016, **8**, 2238.

2 Y. T. Han, X. Wu, Y. L. Ma, L. H. Gong, F. Y. Qu and H. J. Fan, *CrystEngComm*, 2011, **13**, 3506.

3 L. N. Gao, F. Y. Qu and X. Wu, *J. Mater. Chem. A*, 2014, **2**, 7367–7372.

4 N. Chen, Y. Gao, M. N. Zhang, X. Meng, C. Z. Wang, Y. J. Wei, F. Du and G. Chen, *Chem.–Eur. J.*, 2016, **22**, 7248.

5 Y. Liu, Y. Jiao, H. Y. Zhou, X. Yu, F. Y. Qu and X. Wu, *Nano-Micro Lett.*, 2015, **7**, 12.

6 L. N. Gao, X. F. Wang, Z. Xie, W. F. Song, L. J. Wang, X. Wu, F. Y. Qu, D. Chen and G. Z. Shen, *J. Mater. Chem. A*, 2014, **2**, 7167–7173.

7 M. L. Li, Y. Gao, N. Chen, X. Meng, C. Z. Wang, Y. Q. Zhang, D. Zhang, Y. J. Wei, F. Du and G. Chen, *Chem.–Eur. J.*, 2016, **22**, 11405.

8 J. Wei, F. Hu, S. Y. Yao, Z. P. Sun and X. Wu, *Mater. Res. Bull.*, 2017, **93**, 303.

9 X. H. Xiong, G. H. Wang, Y. W. Lin, Y. Wang, X. Ou, F. H. Zheng, C. H. Yang, J. H. Wang and M. L. Liu, *ACS Nano*, 2016, **10**, 10953.

10 X. Ou, X. H. Xiong, F. H. Zheng, C. H. Yang, Z. H. Lin, R. Z. Hu, C. Jin, Y. Chen and M. L. Liu, *J. Power Sources*, 2016, **325**, 410.

11 Y. Y. Zhao, Z. X. Wei, Q. Pang, Y. J. Wei, Y. M. Cai, Q. Fu, F. Du, A. Sarapulova, H. Ehrenberg and B. B. Liu, *ACS Appl. Mater. Interfaces*, 2017, **9**, 4709.

12 Z. J. Zhang, Y. X. Wang, S. L. Chou, H. J. Li, H. K. Liu and J. Z. Wang, *J. Power Sources*, 2015, **280**, 107.

13 N. Yabuuchi, K. Kubota, M. Dahbi and S. Komaba, *Chem. Rev.*, 2014, **114**, 11636.

14 Y. J. Fang, L. F. Xiao, J. F. Qian, X. P. Ai, H. X. Yang and Y. L. Cao, *Nano Lett.*, 2014, **14**, 3539.

15 D. Z. Kong, C. W. Cheng, Y. Wang, B. Liu, Z. X. Huang and H. Y. Yang, *J. Mater. Chem. A*, 2016, **4**, 11800.

16 A. Q. Pan, J. G. Zhang, Z. M. Nie, G. Z. Cao, B. W. Arey, G. S. Li, S. Q. Liang and J. Liu, *J. Mater. Chem.*, 2010, **20**, 9193.

17 M. Winter, J. O. Besenhard, M. E. Spahr and P. Novák, *Adv. Mater.*, 1998, **10**, 725.

18 H. N. He, G. H. Jin, H. Y. Wang, X. B. Huang, Z. H. Chen, D. Sun and Y. G. Tang, *J. Mater. Chem. A*, 2014, **2**, 3563.

19 H. N. He, Z. G. Shang, X. B. Huang, S. Tan, D. Sun, G. Q. Xu, Y. G. Tang and H. Y. Wang, *J. Electrochem. Soc.*, 2016, **163**, A2349.

20 G. Q. Xu, H. N. He, H. Wan, R. H. Liu, X. G. Zeng, D. Sun, X. B. Huang and H. Y. Wang, *J. Appl. Electrochem.*, 2016, **46**, 879.

21 J. K. Kim, B. Senthilkumar, H. S. Sun, J. H. Kim, M. F. Chi and Y. Kim, *ACS Appl. Mater. Interfaces*, 2015, **12**, 7025.

22 S. A. Bach, *J. Electrochem. Soc.*, 1990, **137**, 1042.

23 S. Q. Liang, J. Zhou, G. Z. Fang, C. Zhang, J. Wu, Y. Tang and A. Q. Pan, *Electrochim. Acta*, 2014, **130**, 119.

24 D. Sun, G. H. Jin, H. Y. Wang, P. Liu, Y. Ren, Y. F. Jiang, Y. G. Tang and X. B. Huang, *J. Mater. Chem. A*, 2014, **2**, 12999.

25 Y. K. Lu, J. Wu, J. Liu, M. Lei, S. S. Tang, P. J. Lu, L. Y. Yang, H. R. Yang and Q. Yang, *ACS Appl. Mater. Interfaces*, 2015, **7**(31), 17433.

26 Q. G. Tan, Y. P. Wang, Y. Tang, X. P. Tan, S. Q. Liang and G. Z. Cao, *CrystEngComm*, 2015, **17**, 4774.

27 D. L. Jiang, H. Wang, G. P. Li, G. Q. Li, X. Z. Lan, M. H. Abib, Z. P Zhang and J. G. Yang, *J. Electrochem. Soc.*, 2015, **162**(4), A697.

28 P. P. Wang, Y. X. Cheng, F. X. Ma, Y. Li and L. Zhen, *RSC Adv.*, 2016, **6**, 105833.

29 H. N. He, X. G. Zeng, H. Y. Wang, N. Chen, D. Sun, Y. G. Tang, X. B. Huang and Y. F. Pana, *J. Electrochem. Soc.*, 2015, **162**(1), A39.

30 M. S. Park, Y. M. Kang, G. X. Wang, S. X. Dou and H. K. Liu, *Adv. Funct. Mater.*, 2008, **18**, 455.

31 Y. Liu and X. G. Zhang, *Electrochim. Acta*, 2009, **54**, 4180.

32 I. Seo, G. C. H. Wang, J. K. Kim and Y. Kim, *Electrochim. Acta*, 2016, **193**, 160.

33 Y. H. Cao, D. Fang, C. Wang, L. C. Li, W. L. Xu, Z. P. Luo, X. Q. Liu, C. X. Xiong and S. Q. Liu, *RSC Adv.*, 2015, **5**, 42955.

34 S. L. Zheng, X. Y. Wang, H. Yan, H. Du and Y. Zhang, *Mater. Res. Bull.*, 2016, **81**, 10.

35 H. M. Liu, H. S. Zhou, L. P. Chen, Z. F. Tang and W. S. Yang, *J. Power Sources*, 2011, **196**, 814.

36 X. Y. Wang, Q. Liu, H. Wang, D. L. Jiang, Y. J. Chang, T. Zhang, B. Zhang, H. H. Mou and Y. Jiang, *J. Mater. Sci.*, 2016, **51**, 8986.

37 Y. K. Lu, N. Su, L. Z. Cheng, J. Liu, L. Y. Yang, H. R. Yang, Q. Yang, S. T. Li, J. Min and M. Lei, *Mater. Lett.*, 2016, **183**, 346.

38 Y. Zhu, Y. Xu, Y. Liu, C. Luo and C. Wang, *Nanoscale*, 2013, **5**(2), 780.